Dissociative Photoionization of $X(CH_3)_3$ (X = N, P, As, Sb, Bi): Mechanism, Trends, and Accurate Energetics

Balázs Hornung,[†] Andras Bodi,[‡] Csaba I. Pongor,[†] Zsolt Gengeliczki,[†,§] Tomas Baer,[||] and Bálint Sztáray*,[⊥]

Institute of Chemistry, Eötvös University, Budapest, 1117, Hungary, Molecular Dynamics Group, Paul Scherrer Institut, 5232 Villigen, Switzerland, Department of Chemistry, University of North Carolina, Chapel Hill, North Carolina 27599, and Department of Chemistry, University of the Pacific, Stockton, California 95211

Received: January 31, 2009; Revised Manuscript Received: April 16, 2009

Threshold photoelectron photoion coincidence spectroscopy is used to study the dissociation of energy-selected $X(CH_3)_3^+$ ions (X = As, Sb, Bi) by methyl loss, the only process observed up to 2 eV above the ionization energy. The ion time-of-flight distributions and the breakdown diagrams are analyzed in terms of the statistical RRKM theory to obtain accurate ionic dissociation energies. These experiments complement previous studies on analogous trimethyl compounds of the N group where X = N and P. However, trimethylamine was observed to lose only an H atom, whereas trimethylphosphine was shown to lose methyl radical, H atom, and, to a lesser extent, methane in parallel dissociation reactions. Both kinetic and thermodynamic arguments are needed to explain these trends. The methyl radical loss has two channels: either a H transfer to the central atom, followed by CH_3 loss, or a direct homolytic bond cleavage. However, the H transfer channel is blocked in trimethylamine by an H loss channel with an earlier onset, and, thus, the methyl loss is not observed. Bond energies are defined based on *ab initio* reaction energies and show that the main thermodynamic reason behind the trends in the energetics is the significantly weakening C=X double bond in the ion in the N → As direction. The first adiabatic ionization energies of $Sb(CH_3)_3$ and $Bi(CH_3)_3$ have also been measured by ultraviolet photoelectron spectroscopy to be 8.02 ± 0.05 and 8.08 ± 0.05 eV, respectively.

Introduction

Although the chemical properties of homologous compounds are often similar, small changes in the electronic structure can result in large differences in chemical properties. We discovered one such case during the investigation of the dissociation patterns of trimethylamine and trimethylphosphine ions.[1,2] While energy-selected trimethylamine ions lose exclusively an H atom, forming $H_2C{=}N(CH_3)_2^+$ ions (isoelectronic with isobutene) over a large internal energy range, the trimethylphosphine ions dissociate not only by H atom loss but also via methyl and methane loss, the methyl loss being the lowest energy and dominant channel. The methyl loss channel can involve a simple X−C bond break to form $X(CH_3)_2^+$ or can take place via a prior H atom transfer step to produce the pentavalent intermediate, $(CH_3)_2X(H){=}CH_2^+$, followed by methyl loss to finally produce the tetravalent $(CH_3)(H)X{=}CH_2^+$ ion. An overview of these processes is presented in Figure 1. The difference in the products for the trimethylamine and phosphine cannot be explained by the thermodynamics of the product species, as the calculated stability differences between the H atom loss and an H transfer followed by CH_3 loss (the preferred path for methyl loss in these species) suggest a strong preference for the latter in trimethylamine, the opposite of what is observed. Therefore, explaining the trends in the dissociation pattern involves not only knowing how bond energies change from the second to the third row central atom but also kinetic arguments.

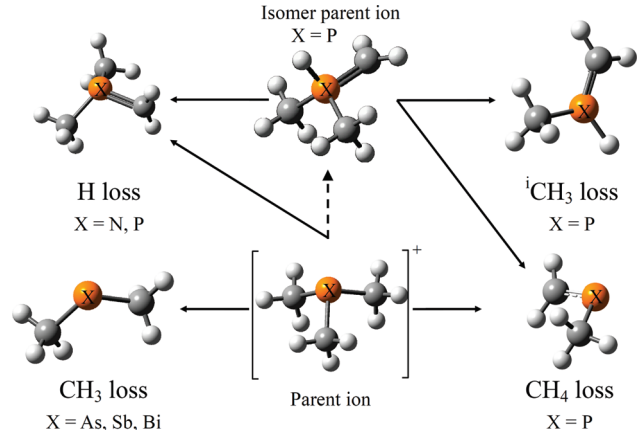

Figure 1. Possible dissociation reaction schemes for $X(CH_3)_3^+$ (X = N, P, As, Sb, Bi) at low internal energies.

In order to shed more light on this trend, we have embarked on a study of three higher mass homologues: trimethylarsane, -stibane, and -bismane, which completes the series $X(CH_3)_3$, X = N, P, As, Sb, Bi. As in the previous study, ions are produced in the gas phase, and energy selected by threshold photoelectron photoion coincidence (TPEPICO) using a monochromatic photon beam in the vacuum UV range from 7 to 14 eV.[3−10] The ion internal energy in a photoionization process is given by $E_{ion} = h\nu + E_{th} - IE - E_{el}$, where the quantities are the photon energy, the neutral molecule's thermal energy, the adiabatic ionization energy, and the electron kinetic energy, respectively. By measuring the ions in coincidence with initially

* Author to whom correspondence should be addressed. E-mail: bsztaray@pacific.edu.
[†] Eötvös University.
[‡] Paul Scherrer Institut.
[§] Current address: Department of Chemistry, Stanford University, Stanford, CA 94305.
[||] University of North Carolina.
[⊥] University of the Pacific.

zero-energy electrons (threshold electrons), the ion is effectively energy selected. The time-of-flight (TOF) mass spectra as a function of the photon energy provide information about the ion dissociation energies. The data are then analyzed with the aid of *ab initio* calculations of the various reaction paths.

Experimental Section

Trimethylarsane was purchased from Sigma-Aldrich and used without further purification. Trimethylstibane was synthesized according to Fleming:[11] antimony trichloride was purified by vacuum sublimation; 25.4 g (0.111 mol) of the halide was dissolved in 55 cm^3 of diethyl ether and added to a 190 cm^3 ether solution of methylmagnesium iodide (0.334 mol). The reaction mixture was subjected to fractional distillations in order to obtain pure trimethylstibane (16.5 g, 88% yield). Trimethylbismane was prepared similarly via the method described by Amberger:[12] a solution made of 33.1 g (0.105 mol) of dry bismuth(III) chloride and 250 cm^3 of diethyl ether was added dropwise to a methylmagnesium iodide solution (0.320 mol in 190 cm^3 diethyl ether). The reaction product was purified with fractional distillation to produce 18.1 g of trimethylbismane (68% yield).

Photoelectron Spectroscopy. In order to overcome the significant uncertainty concerning the adiabatic IEs, photoelectron spectra were recorded for $Sb(CH_3)_3$ and $Bi(CH_3)_3$, using He(I) radiation with the ATOMKI ESA-32 UV photoelectron spectrometer, equipped with a Leybold-Heraeus UVS 10/35 high-intensity gas discharge photon source and a hemispherical analyzer.[13] The energy resolution was better than 30 meV, and the sample was introduced through a gas inlet system at room temperature. Nitrogen was used as an internal standard.

Threshold Photoelectron Photoion Coincidence (TPEPICO). The TPEPICO apparatus at the University of North Carolina is only briefly presented, as it has been described in detail elsewhere.[14,15] The sample is introduced in the ionization chamber through an inlet needle. The sample gas was in thermal equilibrium with the inlet system; therefore, room temperature was assumed in the data analysis. Vacuum UV light from a hydrogen discharge lamp dispersed by a 1 m normal incidence monochromator is used to ionize the gas-phase thermal sample. The wavelength resolution of 1 Å translates to 8 meV (0.8 kJ mol^{-1}) at the onset energies obtained in this study (approximately 10 eV). The photon energy was calibrated using the intense Lyman-α emission line of the light source at 1215.67 Å. Electrons and ions are accelerated out of the ionization region in a homogeneous 20 V cm^{-1} field. Threshold electrons are velocity focused along the extraction axis onto a 1.5 mm aperture located 12 cm from the ionization region and detected by a Channeltron electron multiplier. Because energetic electrons with initial velocity vectors directed parallel to the extraction axis are also focused onto this aperture, the threshold electron signal is contaminated with "hot" electrons. They are accounted for by collecting a second set of electrons, whose trajectory ends in a 2 mm × 5 mm rectangular aperture close to the central aperture where a second Channeltron detects them. Electrons collected by the off-axis rectangular aperture have been found to be a good representation of the hot electrons at the central collector,[16] so that the off-axis signal can be used to correct for hot electron contamination to yield a pure threshold electron signal.

Ions are accelerated in the constant 5 cm long 20 V cm^{-1} field to −100 V, and then within 5 mm to −260 V as they enter the main drift region of the linear time-of-flight analyzer. The ions travel through a 26 cm long field-free drift region and are detected by tandem Burle multichannel plates. The two electron signals are fed into two Ortec 467 time-to-pulse height converters and used as start signals for the ion TOF measurement, and the ion TOF distributions are obtained for both the central and the off-axis electron signals with Ortec TRUMP-8K multichannel analyzers.

The purpose of the 5 cm long acceleration region is to disperse slowly dissociation ions into asymmetric fragment ion peaks, the shape of which provides information about the ion dissociation rates in the 10^4-10^7 s^{-1} range. In order to extend the rate measurements to 10^3 s^{-1}, it is possible to decelerate ions some 20 cm into the drift region.[17] Without this deceleration stage, daughter ions formed in the field-free region have the same time-of-flight as their parents. But because their mass is smaller, they can be decelerated more than the parent ions and thus distinguished from them. This extends rate information to nearly the full parent ion TOF.

The experimental results consist of the ion TOF distributions at various photon energies. The fractional abundances of the various parent and fragment ions were corrected for the hot electron contribution and plotted as a function of the photon energy to produce the breakdown diagram. In some cases, the TOF distribution of the fragment ion exhibited an asymmetry, which is characteristic of slow dissociations. The peak shapes are modeled to obtain the ion dissociation rate constants as a function of the ion internal energy.

Results and Discussion

Adiabatic Ionization Potentials. In order to model the slow dissociation rates, it is necessary to know the molecule's adiabatic ionization energy to determine an accurate E_{ion}. This is well established for $N(CH_3)_3$ but progressively less well-known for the higher homologues.[18] Elbel et al. recorded the He(I) spectra of trimethylarsane and reported a vertical ionization energy of 8.65 eV.[19] An adiabatic IE of 8.2 eV was derived based on his spectrum by the NIST Chemistry Webbook.[18] Cullen and Frost[20] determined the $As(CH_3)_3^+$ cation's lowest appearance energy with Warren's extrapolated voltage difference method,[21] which yielded an adiabatic IE of 8.3 ± 0.1 eV. We carried out a composite G2[22] calculation to confirm this value that yielded 8.287 eV for the adiabatic IE for $As(CH_3)_3^+$. This agrees quite well with the previous experimental values; therefore, we chose to use Cullen and Frost's result in the RRKM model of the dissociation.

There have been two different adiabatic IE values published for trimethylstibane. First is the 7.7 eV value derived from Elbel's[19] paper in the NIST database. Second, Winters and Kiser[23] determined an appearance energy of 8.04 ± 0.16 eV for the $Sb(CH_3)_3^+$ cation with Warren's method. To the best of our knowledge, no adiabatic IE has been published for trimethylbismane.

The photoelectron spectra recorded for $Sb(CH_3)_3$ and $Bi(CH_3)_3$, using He(I) radiation with the ATOMKI ESA-32 UV photoelectron spectrometer, are shown in Figure 2. A detailed assignment of the trimethylarsane and trimethylbismane photoelectron spectra can be found in the literature.[19,24] The first bands in Figure 2 correspond to ionization from the central atom's lone pair. The measured vertical ionization energies of $Sb(CH_3)_3$ and $Bi(CH_3)_3$ are 8.47 ± 0.03 and 8.44 ± 0.03 eV, respectively, which agree with Elbel's data.[19]

The adiabatic ionization energy can be estimated with the low-energy limit of the first peak in the photoelectron spectrum, i.e., the sum of the baseline plus the double of its standard deviation for a statistically significant upper limit to the adiabatic

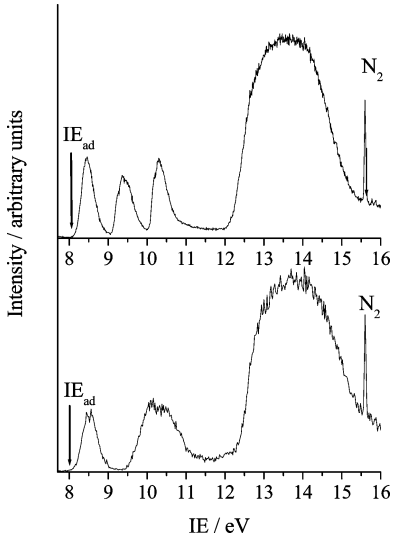

Figure 2. He(I) photoelectron spectra of $Sb(CH_3)_3$ and $Bi(CH_3)_3$ with adiabatic ionization energies.

IE. The lone pair peaks were recorded with a better S/N ratio and fitted in order to determine the adiabatic ionization energies. The Shirley background[25] was chosen to model the baseline, and the peaks were fitted with a pseudo-Voigt function[26] using the simplex algorithm. By applying this approximation, the adiabatic ionization energies for $Sb(CH_3)_3$ and $Bi(CH_3)_3$ are measured to be 8.02 ± 0.05 and 8.08 ± 0.05 eV, respectively.

One can relate the difference in the adiabatic and vertical ionization energies to the geometry change upon ionization. The trend (from N to Bi: 0.7, 0.5, 0.35, 0.45, and 0.36 eV) is in line with the qualitative arguments based on the hybridization of the lone pair (see later). The noise in the trend between As and Sb is probably also due to the uncertainties in the adiabatic IEs.

Threshold Photoelectron Photoion Spectroscopy. ***Trimethylarsane.*** TPEPICO TOF spectra for trimethylarsane were recorded at 32 photon energies in the 10.6−12.9 eV energy range. As shown in Figure 3, at energies below 12 eV, the parent ion only loses a methyl radical to form $As(CH_3)_2^+$ (*m*/*z* of 105.0), a peak that is observed at a TOF of 22.33 μs. It is evident that the methyl loss fragment peak is asymmetric, which indicates that the parent ion dissociates during the whole length of the first 5 cm long acceleration region. At low photon energies, ions continue to dissociate in the 20 cm long drift region. A final deceleration region slows the fragment ions more than the parent ions, thus permitting us to distinguish these drift fragment ions by the peak at 24.63 μs. The fragment ion peak shapes become progressively more symmetric as the photon energy is increased because its dissociation rate constant is a strongly increasing function of the ion internal energy. The breakdown diagram for the methyl loss from $As(CH_3)_3^+$ between 10.6 and 11.3 eV is shown in Figure 4 together with the RRKM fit.

A new reaction pathway arises at higher energies, and a new peak can be observed in the TOF spectrum recorded at 12.7 eV (not shown in Figure 3), as a shoulder on the daughter ion peak at 22.12 μs. This peak, corresponding to a mass *m*/*z* of 102.9, is assigned to the $AsC_2H_4^+$ ion, which can be produced by consecutive CH_4 and H or CH_3 and H_2 loss in this energy range. The missing CH_4 and H loss signal and the shape of the breakdown diagram (not shown) indicate that this product arises from the consecutive $As(CH_3)_2^+ \rightarrow AsC_2H_4^+ + H_2$ reaction. Quantum chemical calculations suggest that the product ion has a bridged ethene structure.

Trimethylstibane. Coincidence spectra were recorded at 24 photon energies between 9.9 and 10.5 eV, and a typical TOF distribution at 10.15 eV is shown in Figure 3. The double peak at 25.89 and 26.05 μs belongs to the parent ion, and the relative

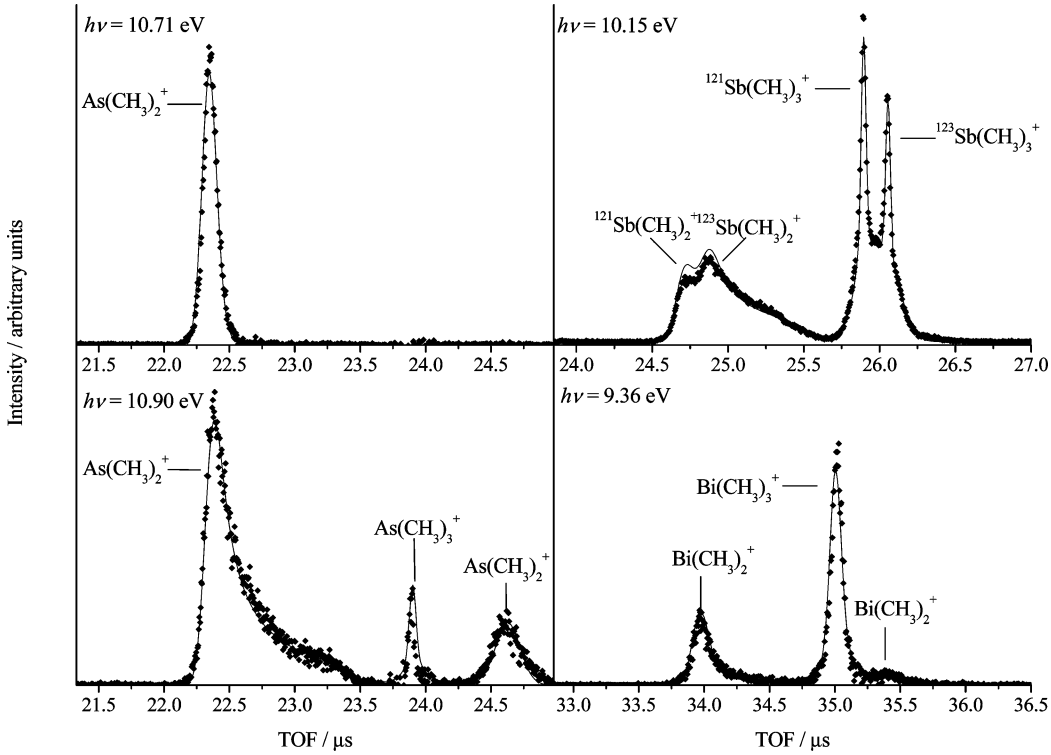

Figure 3. Time-of-flight distributions for trimethylarsane, trimethylstibane, and trimethylbismane. The asymmetric daughter ion peak shapes permit the direct measurement of the rate constant of the photodissociation. The use of the two-stage linear TOF for $As(CH_3)_3^+$ and $Bi(CH_3)_3^+$ distinguishes parents from daughter ions formed in the first field-free drift region. The latter are detected at a higher time-of-flight.

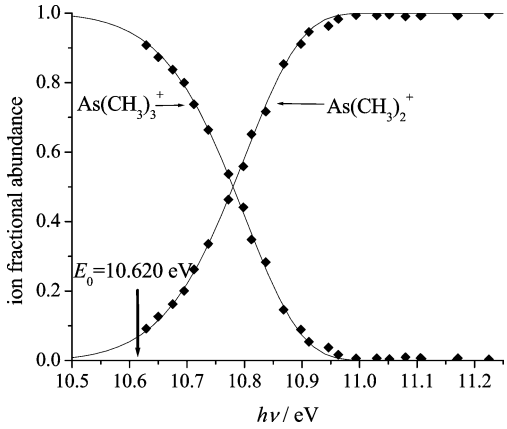

Figure 4. Breakdown diagram for $As(CH_3)_3^+$. The fractional abundances are obtained by calculating the TOF peak integrals and correcting for the hot electron contamination. Dots correspond to experimental values; the continuous line is the RRKM model at $T = 298$ K.

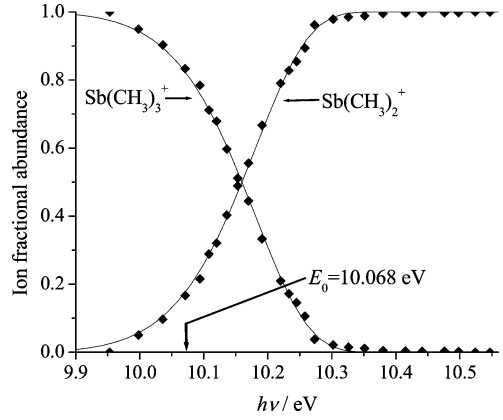

Figure 5. Breakdown diagram for $Sb(CH_3)_3^+$.

peak heights correlate with the natural relative abundance of antimony isotopes (^{121}Sb 57.4%, ^{123}Sb 42.6%). Daughter ion peaks are seen at 24.68 and 24.86 μs.

The only observed photodissociation reaction in this energy range is the loss of a methyl radical. The asymmetry of the daughter ion peak, resulting from the slow dissociation, distorts the isotope peak heights. However, they are faithfully reproduced by the modeled TOF distribution (solid line). No fragment ion drift peak is observed after the parent ion because, as the rate constants increase steeper than was the case for trimethylarsane, it was not necessary to decelerate the ions in order to obtain an accurate onset energy. The breakdown diagram is shown in Figure 5.

Trimethylbismane. Experimental data were collected between 9.2 and 9.6 eV at 26 photon energies. We obtained three peaks in this energy range (Figure 6). The parent ion appears at 34.89 μs, and the wide peak at 35.42 μs is the drift peak. The daughter ion with m/z ratio of 239 at 33.98 μs corresponds to methyl radical loss, which is the sole reaction pathway in this energy region. Of the three compounds investigated in this study, the trimethylbismane ion dissociates most rapidly and is, thus, barely metastable. The breakdown diagram of the methyl loss is shown in Figure 6.

Computations. Ab initio calculations were carried out with the Gaussian03[27] and ACESII[28] (Mainz version) program suites. The room temperature thermal distribution and the RRKM dissociative photoionization rate constants are based on the densities of states for the parent molecule, parent ion, and numbers of states for the transition states. These are, in turn,

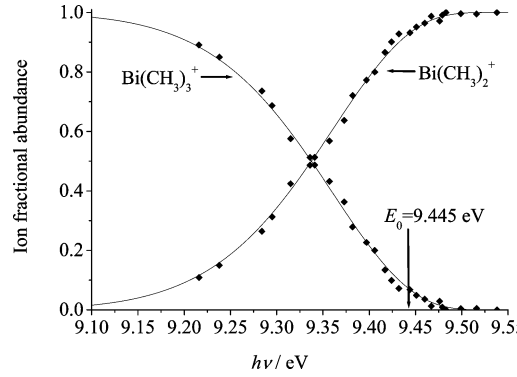

Figure 6. Breakdown diagram for $Bi(CH_3)_3^+$.

based on vibrational levels and rotational constants, which were calculated with density functional theory using the B3LYP exchange-correlation functional and Pople's 6-311++G(d,p) basis set for H, C, and As atoms. The basis sets for Sb and Bi were the double-ζ, polarization-augmented LANL2dzdp with effective core potentials from Hay, Wadt, and Check.[29−31] The transition state geometry and initial frequencies in the RRKM fit were determined by carrying out constrained geometry optimizations at fixed C−X bond lengths in the 3−7 Å range. The vibrational frequencies obtained from these calculations were used as starting points in the RRKM modeling, fitted to reproduce the experimentally observed rate curves.

Two-dimensional potential energy surfaces (PESs) for H transfer in the parent ion along a C−H bond length and the H−C−X bond angle and *ab initio* energetics were also calculated in order to explain the photodissociation pathways previously observed in $N(CH_3)_3^+$ and $P(CH_3)_3^+$, and to determine if the methyl loss product from $X(CH_3)_3^+$ (X = As, Sb, Bi) corresponds to $X(CH_3)_2^+$ or the isomerized $(CH_3)(H)X{=}CH_2^+$ structure. The computational cost of obtaining these surfaces proved to be prohibitive for the trimethyl compounds other than trimethylamine. However, we found that the PES for the isomerization $N(CH_3)_3^+ \rightarrow HN(CH_3)_2(CH_2)^+$ at the MP2/cc-pVTZ level was very similar to that for $NH_2(CH_3)^+ \rightarrow NH_3(CH_2)^+$. Therefore, these calculations were carried out for the monomethyl model compound analogues at the CCSD/cc-pVTZ //CCSD/cc-pVTZ level. The PES was constructed in the following way: 220, 100, 110, and 120 constrained optimizations were carried out for $NH_2(CH_3)^+$, $PH_2(CH_3)^+$, $AsH_2(CH_3)^+$, and $N(CH_3)_3^+$, respectively. A two-dimensional spline fit[32] was used to smooth the raw surface and obtain the PESs shown in Figure 7. A comparison between the calculated energies of parent and possible daughter ions was explored by composite methods. Figure 8 shows the *ab initio* energetics of the ions and their products. CBS-APNO (X = N),[33] G3 (X = N, P),[34] and G2[22] (X = N, P, As) calculations were carried out and found to agree well. The trends in the G2 values, shown in Figure 8, will be discussed later.

Data Analysis. The rate constants used in the analysis of the experimental data were calculated within the RRKM framework. The energy distributions of the parent ions were calculated from the initial thermal energy of the neutral sample, the photon energy, and the ionization energy. The thermal energy distribution is calculated from the neutral vibrational frequencies and rotational constants obtained with density functional theory. The ionization energies were taken from the literature for $As(CH_3)_3$ (8.3 ± 0.1 eV).[19] For $Sb(CH_3)_3$ and for $Bi(CH_3)_3$, the newly determined values of 8.02 ± 0.05 and 8.08 ± 0.05 eV are used. The density of states of the parent ion is based on vibrational frequencies obtained from *ab initio*

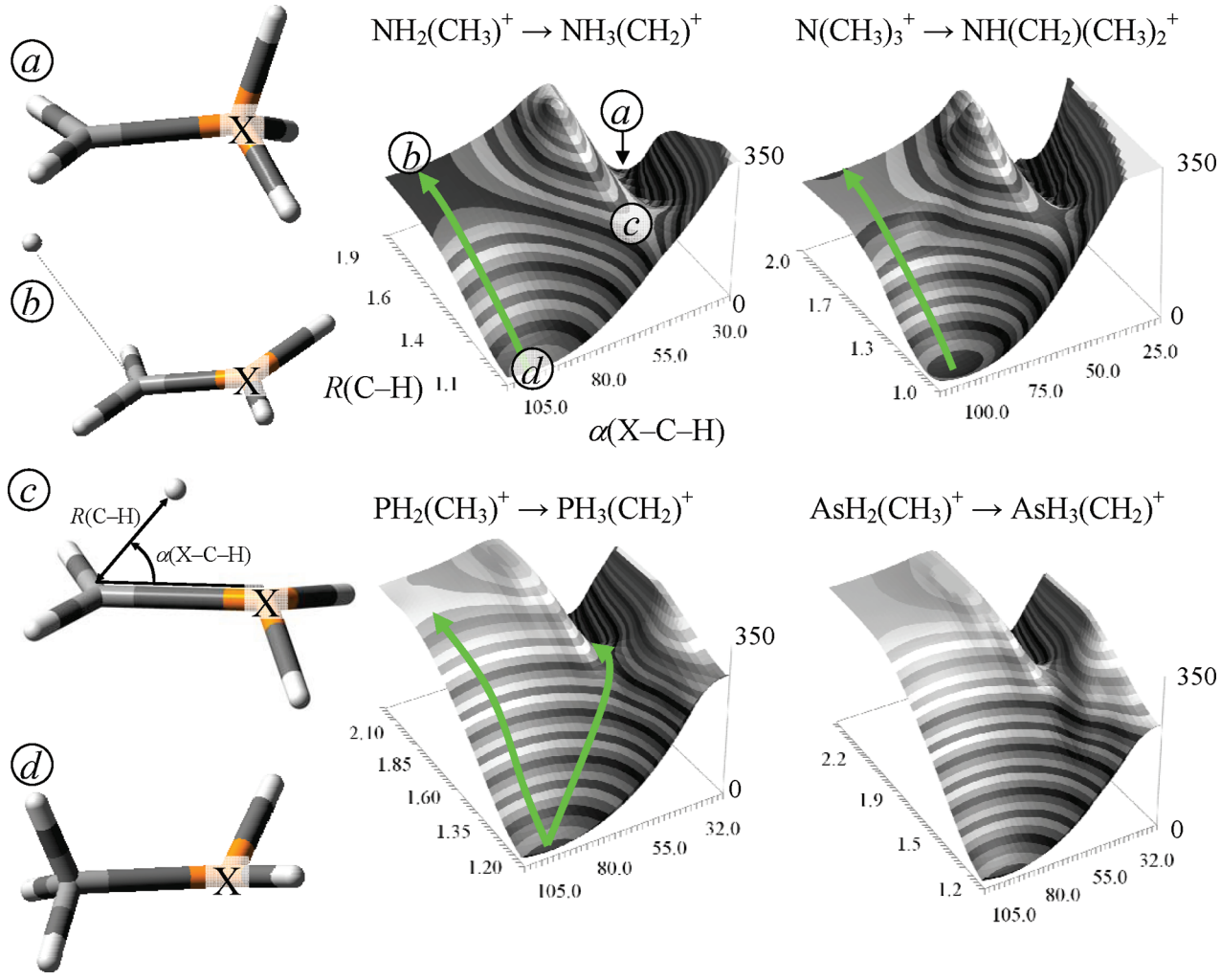

Figure 7. Potential energy surfaces for $N(CH_3)_3^+$, and for the model compounds $NH_2(CH_3)^+$, $PH_2(CH_3)^+$, and $AsH_2(CH_3)^+$. Structure a corresponds to the H transfer isomer parent ion, b to H atom loss, c to the transition state in the H transfer, and d to the parent ion. The PES is acquired along two coordinates preserving the C_S symmetry, and scanning a C−H bond length, and the X−C−H bond angle. For methylamine and trimethylamine, the H transfer barrier exceeds the H atom loss energy, and no isomerization takes place. For the phosphorus compound, isomerization may take place before losing a H atom. Hence, methyl radical loss, H atom loss, and, to a small extent, methane loss may occur simultaneously. The barrier to isomerization and to H atom loss are both too high in the arsenic compound; it loses a methyl radical by homolytic bond cleavage at lower energies.

calculations, so that the only variable parameters in the model are the barrier to dissociation and the lowest five transition state (TS) frequencies that correspond to free rotations and translations in the products. The TOF distributions and the breakdown diagram were modeled using the known sample thermal energy distribution and experimental parameters (acceleration and drift distances and applied voltages), but varying the lowest five transition state frequencies and dissociation energies in order to obtain the best fit to the experimental data.

The RRKM fit to the experiment yielded onset energies for methyl radical loss of 10.620 ± 0.041, 10.068 ± 0.074, and 9.445 ± 0.064 eV for $As(CH_3)_3$, $Sb(CH_3)_3$, and $Bi(CH_3)_3$, respectively. These 0 K onsets are indicated as arrows in Figures 4−6. Note how the 0 K onsets shift with respect to the crossover point, due to kinetic shift. In the case of $As(CH_3)_3$ and $Sb(CH_3)_3$, the 0 K onsets are far to the left of the crossover energy, indicating substantial kinetic shifts. For the bismuth compound, however, the 0 K onset shows negligible kinetic shift. This is in line with the rate curves in Figure 9, as discussed below. The errors in the 0 K onsets were determined by multiplying and dividing the transition state frequencies with various factors, fitting the barrier, and checking for the response of the fit to the assumed set of frequencies. The errors in barriers and the activation entropies were then established by where the fit became unacceptable. This method yielded the following confidence intervals for the methyl loss activation entropies: $\Delta S^{\ddagger} = 69 \pm 23$, 64 ± 17, and 101 ± 45 J mol^{-1} K^{-1} for $As(CH_3)_3^+$, $Sb(CH_3)_3^+$, and $Bi(CH_3)_3^+$ at $T = 600$ K, respectively. The adiabatic ionization energies subtracted from the onset energies yield the homolytic X−C bond energies in $X(CH_3)_3^+$ for X = As, Sb, and Bi, i.e., 224 ± 11, 198 ± 9, and 132 ± 8 kJ mol^{-1}, respectively, as shown in Figure 8. This can be compared with the G2 value of 256 kJ mol^{-1} for $As(CH_3)_3^+$.

The onset for $Sb(CH_3)_3^+$ is nearly 0.5 eV below the 10.5 ± 0.2 eV onset reported by Winter,[23] which is based on a differential voltage extrapolation method, where the intensity of an ion produced from a compound with unknown appearance energy is recorded simultaneously with that of a compound of known appearance energy against the electron beam voltage. Such discrepancies are not unusual when photoionization results are compared with electron ionization onsets.

The rate constants used to fit the TOF distributions and the breakdown diagram, and needed to extrapolate the rates to the dissociation limit, are shown in Figure 9. It is evident

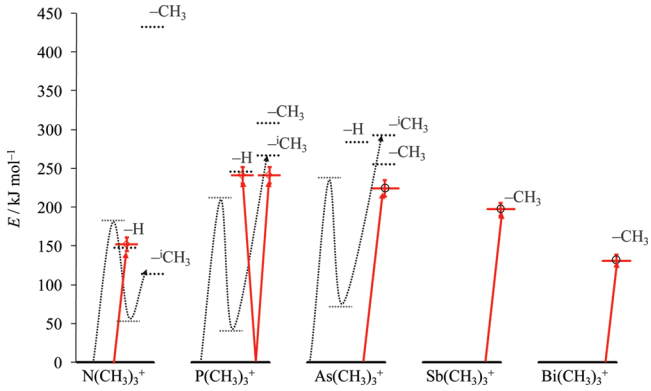

Figure 8. Experimental and *ab initio* reaction energies for H atom loss, methyl loss, and H transfer followed by methyl loss. The experimental H atom loss energy in trimethylamine is from ref 1, the H atom loss energy and the methyl loss energy from the isomer in trimethylphosphine are from ref 2, and the direct methyl loss energies for X = As, Sb, and Bi are from this work. The *ab initio* results are plotted in dotted lines and have been obtained with the G2 method for $N(CH_3)_3^+$, $P(CH_3)_3^+$, and $As(CH_3)_3^+$. The dotted curves show the isomerization pathways. The experimentally observed dissociations are marked with solid arrows and the energies with solid lines.

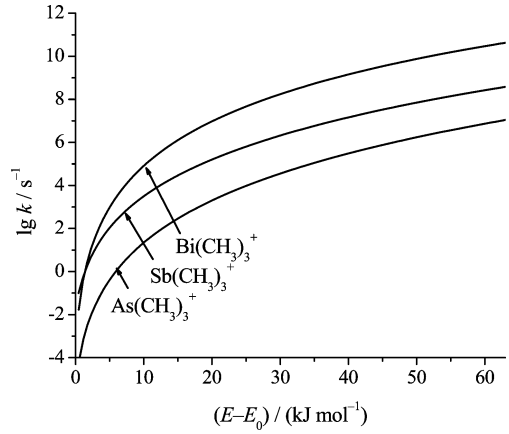

Figure 9. RRKM-fitted rate constants for methyl loss reaction from $X(CH_3)_3^+$ (X = As, Sb, Bi) as a function of ion internal energy above the threshold for the dissociation.

that the metastable energy range ($10^3 < k < 10^6$ s^{-1}) decreases as we go down in the periodic table, and the slope of the rate constant vs internal energy curve increases. This is a result of two factors. On the one hand, the X−CH_3 bond energy decreases from As to Bi. On the other hand, the transition state becomes looser (higher entropy of activation) as well.

Ab Initio Energetics and Potential Energy Surfaces. To summarize the experimental results, only H atom loss is observed for trimethylamine, whereas only CH_3 loss is observed for trimethylarsane, -stibane, and -bismane. However, both H atom as well as methyl loss reactions are observed for trimethylphosphine (the minor methane loss channel is ignored in the discussion). The calculations strongly suggest that the methyl loss channel in the three heavier homologues proceeds via simple homolytic X−CH_3 bond cleavage.

The potential energy surfaces in Figure 7 show the region associated with direct H loss and the H atom isomerization path leading to the isomerized methyl loss product ion, $(CH_3)HX{=}CH_2^+$. For both $N(CH_3)_3^+$ and $NH_2CH_3^+$, the H loss path (d → b) lies about 20 kJ/mol below the transition state for H atom isomerization (structure c). In addition, the direct C−H cleavage reaction has a much higher number of states (looser transition state, or higher entropy of activation) than the H atom isomerization reaction. Thus, even though the isomerized methyl loss product is calculated to lie about 25 kJ/mol below the H loss channel, this path is effectively closed because of the energetic and entropic barrier in the trimethyl- (and monomethyl-) amine ion, as was indeed observed experimentally.[1] It is rather remarkable that it costs less energy to remove an H atom completely than to move it over to the isomerized position. Evidently, this is because of the great stability of the $(CH_3)_2N{=}CH_2^+$ product ion, which depresses this energy relative to the other molecules in this series (see Figure 8).

The picture changes when the central atom is exchanged for phosphorus. The barrier to direct H atom loss increases by more than 100 kJ mol^{-1} according to all calculations, and the H transfer barrier increases by less than 50 kJ mol^{-1}. Therefore, isomerization can take place well before H atom loss is observed, and it is in fact methyl loss from the isomer parent ion that dominates the breakdown diagram, as shown previously.[2]

The PES for H atom transfer in methylarsane shows a slightly higher (by 30 kJ mol^{-1}) activation energy than in methylphosphane, but isomerization in the trimethyl compound becomes impractical at this point, because the direct As−C bond rupture is energetically favored over both the direct H atom loss and the methyl loss from the isomer parent ion. This trend continues, so that only direct methyl loss is observed in the TPEPICO experiments of $As(CH_3)_3$, $Sb(CH_3)_3$, and $Bi(CH_3)_3$.

We can obtain more insight into these trends by decomposing the observed and calculated energies into different types of central atom bonds. Consider the four types of reactions and their G2 calculated reaction energies shown in Figure 10 (for comparison, B3LYP/6-311++G(d,p) values were also obtained and found to agree reasonably well with the G2 data). The reaction energy of H atom loss from methane (within 2 kJ mol^{-1} of the experimental value) was taken as C−H bond energy and kept constant. Three central atom dependent reactions were used to calculate the C−X, C=X, and X−H bond energies according to the following scheme: CH_3 loss from the parent ion via homolytic bond cleavage yields directly the C−X bond energy, H loss from the parent ion involves breaking a C−H bond and a C−X bond and creating a C=X bond, thus yielding the C=X bond energy, and CH_3 loss from the parent ion combined with H atom transfer involves breaking two C−X bonds and a C−H bond and forming a C=X bond and an X−H bond, thus yielding the X−H bond energy. It is possible to assign bond energies to all types of bonds this way and use them to shed light on the thermochemical trends that partly determine the photodissociation mechanism.

The trends in the C−X and C=X bond energies (Figure 10) explain the changes in the dissociation energetics as the central atom becomes larger. C=X bonds weaken significantly more than C−X single bonds in the N → P → As direction, thus leading to a relative destabilization of the daughter ions of H atom loss and methyl radical loss from the isomer parent ion. The destabilization of the double bonds is expected because of the less favorable orbital overlap between the carbon and the central atom as the central atom size increases, and it is its relative magnitude with respect to the single bonds that gives rise to the switchover in the photodissociation energetics in the P → As step.

Another way of looking at the bonding trends is via hybridized bonds. The hybrid state of the parent molecules, $X(CH_3)_3$, is sp^3, which results in a pyramidal structure. The s orbital contribution in the lone pair of the X atoms is larger than in the bonding orbitals, and therefore the lone pair occupies

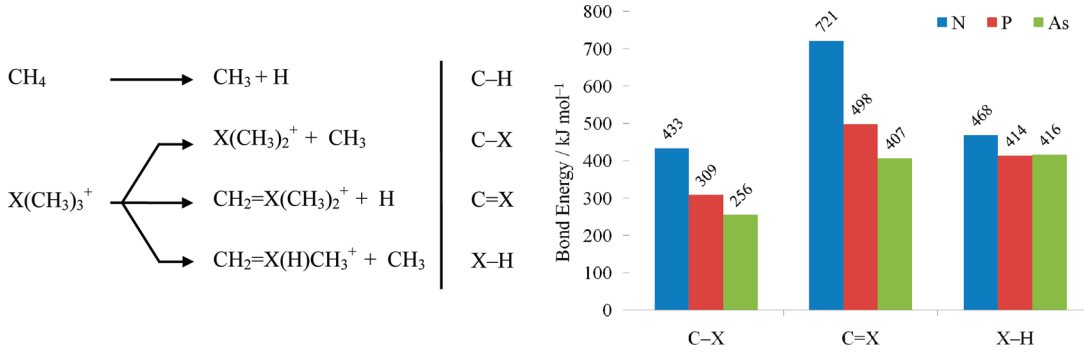

Figure 10. Bond energies derived from G2 reaction energies.

a larger solid angle than the bonding MOs, leading to bond angles less than 109.5°. As the s orbital contribution of the lone pairs increases from N to Bi, the bond angles significantly decrease: from N to Bi, 112°, 99°, 97°, 95°, and 94°; in the case of trimethylbismane it is so close to orthogonal that there is probably very little s AO contribution to the bonding orbitals. This behavior was already predicted by Pauling.[35]

Since the first ionization of these molecules removes the electron from the lone pair orbital, the resulting molecular ion becomes planar for $N(CH_3)_3^+$; i.e., the unpaired electron is on an essentially p type orbital. For the heavier analogues, however, there is significant pyramidalization: the calculated bond angle in $Bi(CH_3)_3^+$ is close to the tetrahedral angle (108−111° depending on the level of theory), although the nonbonding orbital is only half-filled.

Hybridization can be invoked to explain the fact that these heavier analogues disfavor the double bond that would be the result of the H-loss dissociation reaction. In this case, the bonding σ orbitals would come from an sp^2 hybrid, which would require a significant participation of the largely inert *n*s orbital ($n = 4, 5, 6$, respectively, for As, Sb, Bi). Since this s orbital is lower-lying than the p orbitals in the heavier pnictogens due to the inert-pair effect,[36,37] the sp^2 hybrid is energetically disfavored, and the lower-energy methyl dissociation takes place that leads to a divalent ion. In these species, the inert s orbital plays increasingly little role in the bonding. The bond angles for the $CH_3{-}X{-}CH_3^+$ ions, therefore, decrease from X = N over P, As, and Sb to Bi, as 121°, 104°, 101°, 96°, and 95°, respectively (B3LYP/6-311G(d,p) values).

Conclusions

The photoionization/photodissociation mechanism of the trimethylamine to trimethylbismane series was studied by TPEPICO. The slow methyl loss dissocations were modeled with RRKM theory in order to extract the dissociation onsets. The resulting methyl loss onset energies for $As(CH_3)_3$, $Sb(CH_3)_3$, and $Bi(CH_3)_3$ are 10.620 ± 0.041, 10.068 ± 0.074, and 9.445 ± 0.064 eV, respectively, and the corresponding ionic C−X bond energies are found to monotonically decrease with the period number of the central atom (224, 198, and 132 kJ mol^{-1}, respectively). The dissociation energetics and dynamics of the three molecules presented here are compared with previously investigated $N(CH_3)_3$ and $P(CH_3)_3$, thus completing the series from nitrogen to bismuth. *Ab initio* potential energy surfaces for trimethylamine and model monomethyl compounds are shown to clarify why H transfer to the central atom only takes place in the photodissociation of $P(CH_3)_3^+$. C−X, C═X, and X−H bond energies are calculated from *ab initio* reaction energies in the N → P → As series and are used to explain the switchover in the energetics to the direct C−X bond cleavage becoming the most favorable reaction path for $As(CH_3)_3^+$. Therefore, it is competing kinetic and energetic arguments that explain the changing photoionization/photodissociation pattern in energy selected trimethylamine, trimethylphosphine, trimethylarsane, trimethylstibane, and trimethylbismane ions.

Acknowledgment. The computational facilities made available by Prof. Paul Mezey, Scientific Modeling and Simulation Laboratory, Memorial University of Newfoundland, are gratefully acknowledged. A.B. is also thankful for comments from and discussions with Dr. Thomas Gerber. B.S. gratefully acknowledges the support of the Hungarian Science Fund (OTKA #61153). This collaboration was made possible by the grants from the U.S. National Science Foundation, the U.S. Department of Energy, and the Hungarian Science Fund (OTKA #71644).

References and Notes

(1) Bodi, A.; Sztaray, B.; Baer, T. *Phys. Chem. Chem. Phys.* **2006**, *8* (5), 613.
(2) Bodi, A.; Kercher, J. P.; Baer, T.; Sztáray, B. *J. Phys. Chem. B* **2005**, *109*, 8393.
(3) Nishimura, T.; Zha, Q.; Meisels, G. G. *J. Chem. Phys.* **1987**, *87*, 4589.
(4) Weitzel, K. M.; Mähnert, J.; Baumgärtel, H. *Ber. Bunsen-Ges. Phys. Chem.* **1993**, *97*, 134.
(5) Dannacher, J.; Rosenstock, H. M.; Buff, R.; Parr, A. C.; Stockbauer, R.; Bombach, R.; Stadelmann, J. P. *Chem. Phys.* **1983**, *75*, 23.
(6) Norwood, K.; Ali, A.; Flesch, G. D.; Ng, C. Y. *J. Am. Chem. Soc.* **1990**, *112*, 7502.
(7) Duffy, L. M.; Keister, J. W.; Baer, T. *J. Phys. Chem.* **1995**, *99*, 17862.
(8) Thissen, R.; Alcaraz, C.; Hepburn, J. W.; Vervloet, M.; Dutuit, O. *Int. J. Mass Spectrom.* **2000**, *199*, 201.
(9) Weitzel, K. M.; Mähnert, J. *Z. Phys. Chem.* **1996**, *195*, 181.
(10) Li, Y.; Sztáray, B.; Baer, T. *J. Am. Chem. Soc.* **2001**, *123*, 9388.
(11) Fleming, I. *Science of Synthesis: Houben-Weyl Methods of Molecular Transformations: Category 1: Organometallics (Compounds of Group 15 (As, Sb, Bi) and Silicon Compounds)*, 1st ed.; Georg Thieme Verlag: Stuttgart, 2001.
(12) Amberger, E. *Chem. Ber.* **1961**, *94* (6), 1447.
(13) Csakvari, B.; Nagy, A.; Zanathy, L.; Szepes, L. *Magy. Kem. Foly.* **1992**, *98* (10), 415.
(14) Baer, T.; Li, Y. *Int. J. Mass Spectrom.* **2002**, *219*, 381.
(15) Baer, T.; Sztáray, B.; Kercher, J. P.; Lago, A. F.; Bodi, A.; Skull, C.; Palathinkal, D. *Phys. Chem. Chem. Phys.* **2005**, *7*, 1507.
(16) Sztáray, B.; Baer, T. *Rev. Sci. Instrum.* **2003**, *74*, 3763.
(17) Davalos, J. Z.; Koizumi, H.; Baer, T. *J. Phys. Chem. A* **2006**, *110* (15), 5032.
(18) *NIST Chemistry WebBook, NIST Standard Reference Database Number 69, February 2000 ed.*; National Institute of Standards and Technology: Gaithersburg, MD, 2005.
(19) Elbel, S.; Dieck, H. T.; Demuth, R. *J. Fluorine Chem.* **1982**, *19* (3−6), 349.
(20) Cullen, W. R.; Frost, D. C. *Can. J. Chem.* **1962**, *40* (2), 390.
(21) Warren, J. W. *Nature* **1950**, *165* (4203), 810.
(22) Curtiss, L. A.; Raghavachari, K.; Trucks, G. W.; Pople, J. A. *J. Chem. Phys.* **1991**, *94*, 7221.
(23) Winters, R. E.; Kiser, R. W. *J. Organomet. Chem.* **1967**, *10* (1), 7.

(24) Szepes, L.; Nagy, A.; Zanathy, L. PES of organic derivatives of As, Sb and Bi. In *The Chemistry of Organic Arsenic, Antimony and Bismuth Compounds*; Satai, P., Ed.; John Wiley & Sons: New York, 1994; pp 274−280.

(25) Shirley, D. A. *Phys. Rev. B* **1972**, *5* (12), 4709.

(26) Thompson, P.; Cox, D. E.; Hastings, J. B. *J. Appl. Crystallogr.* **1987**, *20*, 79.

(27) Frisch, M. J.; Trucks, G. W.; Schlegel, H. B.; Scuseria, G. E.; Robb, M. A.; Cheeseman, J. R.; Montgomery, J. A.; Vreven, T.; Kudin, K. N.; Burant, J. C.; Millam, J. M.; Iyengar, S. S.; Tomasi, J.; Barone, V.; Mennucci, B.; Cossi, M.; Scalmani, G.; Rega, N.; Petersson, G. A.; Nakatsuji, H.; Hada, M.; Ehara, M.; Toyota, K.; Fukuda, R.; Hasegawa, J.; Ishida, M.; Nakajima, T.; Honda, Y.; Kitao, O.; Nakai, H.; Klene, M.; Li, X.; Knox, J. E.; Hratchian, H. P.; Cross, J. B.; Adamo, C.; Jaramillo, J.; Gomperts, R.; Stratmann, F.; Yazyev, O.; Austin, A. J.; Cammi, R.; Pomelli, C.; Ochterski, J. W.; Ayala, P. Y.; Morokuma, K.; Voth, G. A.; Salvador, P.; Dannenberg, J. J.; Zakrzewski, V. G.; Dapprich, S.; Daniels, A. D.; Strain, M. C.; Farkas, Ö.; Malick, D. K.; Rabuck, A. D.; Raghavachari, K.; Foresman, J. B.; Ortiz, J. V.; Cui, Q.; Baboul, A. G.; Clifford, S.; Cioslowski, J.; Stefanov, B. B.; Liu, G.; Liashenko, A.; Piskorz, P.; Komáromi, I.; Martin, R. L.; Fox, D. J.; Keith, T.; Al-Laham, M. A.; Peng, C. Y.; Nanayakkara, A.; Challacombe, M.; Gill, P. M. W.; Johnson, B.; Chen, W.; Wong, M. W.; Gonzalez, C.; Pople, J. A. *Gaussian 03*, revision C.02; Gaussian, Inc.: Pittsburgh, PA, 2004.

(28) (a) Stanton, J. F.; Gauss, J.; Watts, J. D.; Lauderdale, W. J.; Bartlett, R. J. *Int. J. Quantum Chem., Quantum Chem. Symp.* **1992**, *26*, 879. (b) Stanton, J. F.; Gauss, J.; Watts, J. D.; Lauderdale, W. J.; Bartlett, R. J. ACESII, an ab initio program system including modified versions of the MOLECULE Gaussian integral program of J. Almlöf and P. R. Taylor, the ABACUS integral derivative program written by T. Helgaker, H. J. Aa. Jensen, P. Jørgensen, and P. R. Taylor, and the PROPS property integral code of P. R. Taylor.

(29) Hay, P. J.; Wadt, W. R. *J. Chem. Phys.* **1985**, *82* (1), 270.

(30) Wadt, W. R.; Hay, P. J. *J. Chem. Phys.* **1985**, *82* (1), 284.

(31) Check, C. E.; Faust, T. O.; Bailey, J. M.; Wright, B. J.; Gilbert, T. M.; Sunderlin, L. S. *J. Phys. Chem. A* **2001**, *105* (34), 8111.

(32) XlXtrFun Extra Functions for Microsoft Excel, Advanced Systems Design and Development, Red Lion, PA, 2005. See http://www.xlxtrfun.com/.

(33) Ochterski, J. W.; Petersson, G. A.; Montgomery, J. A. *J. Chem. Phys.* **1996**, *104* (7), 2598.

(34) Curtiss, L. A.; Raghavachari, K.; Redfern, P. C.; Rassolov, V.; Pople, J. A. *J. Chem. Phys.* **1998**, *109* (18), 7764.

(35) Pauling, L. *J. Am. Chem. Soc.* **1931**, *53* (4), 1367.

(36) Freedman, L. D.; Doak, G. O. *Chem. Rev.* **1982**, *82* (1), 15.

(37) Hawley, D. M.; Ferguson, G. *J. Chem. Soc. A* **1968**, (9), 2059.

JP900920R